ABAQUS implementation of a phase field model for pitting corrosion and stress corrosion cracking

Chuanjie Cui[a], Emilio Martínez-Pañeda[b,*]

[a] *College of Civil Engineering, Tongji University, 200092, Shanghai, China*
[b] *Department of Civil and Environmental Engineering, Imperial College London, London SW7 2AZ, UK*

Abstract

Documentation that accompanies the file **PhaseFieldSCC.for**, a user element (UEL) subroutine for implementing the phase field model for dissolution-driven stress corrosion cracking by Cui et al. (2021). The model enables capturing capture pitting corrosion and stress corrosion cracking, incorporating the role of mechanics in enhancing corrosion kinetics and the film-rupture–dissolution–repassivation (FRDR) process. An input file is also provided for demonstration purposes. The files can be downloaded from www.empaneda.com/codes. If using this code for research or industrial purposes, please cite:

C. Cui, R. Ma and E. Martínez-Pañeda, A phase field formulation for dissolution-driven stress corrosion cracking. Journal of the Mechanics and Physics of Solids 147, 104254 (2021), doi: https://doi.org/10.1016/j.jmps.2020.104254.

The main document describes the essential features of the method and provides instructions for using the ABAQUS subroutine. The appendices include details of the theoretical formulation and the finite element framework.

Keywords:
Phase field, Pitting corrosion, Stress corrosion cracking, Passive film, ABAQUS

*Corresponding author.
Email address: e.martinez-paneda@imperial.ac.uk (Emilio Martínez-Pañeda)

1. Phase field FRDR model

The use of an auxiliary phase field is a convenient tool to make the modelling of evolving interfaces amenable to numerical computations. Phase field methods have revolutionised the modelling of various interfacial problems such as microstructural evolution (Provatas and Elder, 2011) and fracture mechanics (see, e.g. Kristensen and Martínez-Pañeda, 2020 and references therein). Here, the phase field paradigm is extended to corrosion; i.e., the phase field variable tracks the evolving interface between the aqueous electrolyte and the solid metal. How the degrading surface of the metal evolves will be driven by two aspects: material dissolution and the rupture of the protective passive film. By capturing these two phenomena we will be able to predict pitting corrosion and stress corrosion cracking.

Our formulation aims at capturing the process of film rupture, dissolution and repassivation. Metals and alloys exposed to conditions of passivation are protected by a nm-size impermeable film of metal oxides and hydroxides that effectively isolates the material from the corrosive environment (Macdonald, 1999). Independently of the specific cracking mechanism, film-rupture is a necessary condition for localised damage in these conditions. Also, a potential rationale for pitting corrosion and stress corrosion cracking is the rupture of the film due to mechanical straining, followed by localised dissolution of the metal (Scully, 1980; Jivkov, 2004). Repassivation follows each local film rupture event, with the new film being deposited on the bare metal under zero-strain conditions. Further input of mechanical work is thus needed to fracture the new film, in a cyclic process governed by the competition between filming and mechanical straining kinetics.

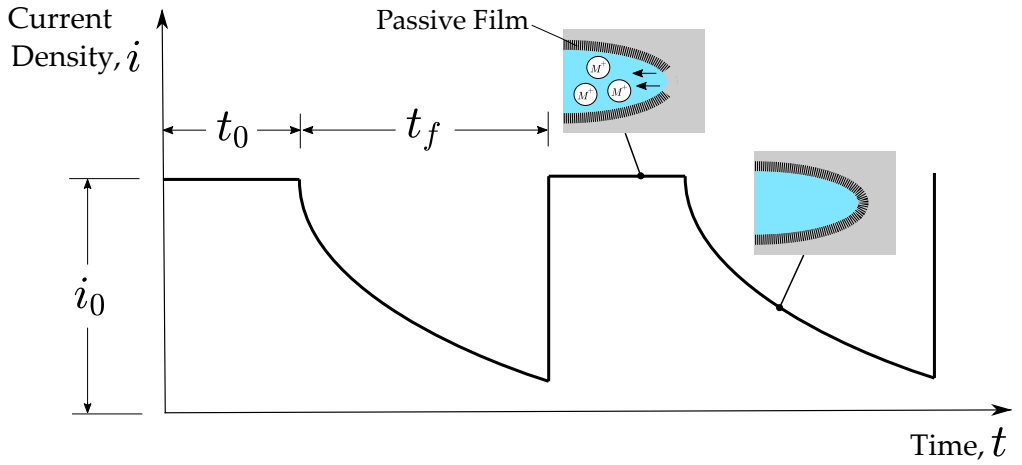

Figure 1: Schematic illustration of two cycles of the film rupture-dissolution-repassivation (FRDR) mechanism at the tip of a defect.

As sketched in Fig. 1, the enhanced corrosion protection resulting from the development of a passive film is characterised by a drop in the corrosion current density i, relative to the corrosion current density associated with bare metal i_0. After a drop time t_f, a film rupture event takes place and the bare metal current density i_0 is immediately recovered. This is followed by a time interval t_0, during which the current flows before decay begins, such that $t_i = t_0 + t_f$ represents one film rupture-dissolution-repassivation cycle. Following common assumptions in the literature (Parkins, 1987), the mechanical work required to achieve film rupture can be characterised using an effective plastic strain quantity, ε^p, such that film rupture will take place when the accumulation of the effective plastic strain over a FRDR interval ε_i^p equals a critical quantity:

$$\varepsilon_i^p = \varepsilon_f \quad \text{with} \quad \varepsilon_i^p = \int_0^{t_i} \dot{\varepsilon}^p \, \mathrm{d}t \tag{1}$$

where $\dot{\varepsilon}^p$ is the effective plastic strain rate and ε_f is the critical strain for film rupture, which is on the order of 0.1% (Gutman, 2007). Thus, the duration of each film rupture-dissolution-repassivation cycle, and the magnitude of t_f, will be dictated by the local values of the equivalent plastic strain and their evolution in time. We proceed to define the degradation of the current density as an exponential function of the time. Thus, during one rupture-

dissolution-repassivation cycle, $i(t_i)$ can be expressed as:

$$i(t_i) = \begin{cases} i_0, & \text{if } \ 0 < t_i \leqslant t_0 \\ i_0 \, \exp\left(-k \left(t_i - t_0\right)\right), & \text{if } \ t_0 < t_i \leqslant t_0 + t_f \end{cases} \tag{2}$$

where k is a parameter that characterises the sensitivity of the corrosion rates to the stability of the passive film, as dictated by the material and the environment.

The role of mechanical stresses and strains is typically restricted to the film rupture event. However, we here consider recent experimental evidence that suggests a further influence of mechanical straining, accelerating corrosion. For example, in Dai et al. (2020) localised corrosion is observed in Q345R steel despite the negligible effect of the passive film in the hydrofluoric acid environment considered. Also, as pointed out by Gutman (2007), localised corrosion rates can be notably accelerated by the influence of residual stresses. Thus, we enhance the definition of the corrosion current density by considering a mechanochemical term k_{m} (Gutman, 1998) as:

$$i_a(t) = k_{\mathrm{m}} \left(\varepsilon^p, \sigma_h\right) i(t_i) = \left(\frac{\varepsilon^p}{\varepsilon_y} + 1\right) \exp\left(\frac{\sigma_h V_m}{RT}\right) i(t_i) \tag{3}$$

where i_a is the mechanochemical corrosion current density, ε^p is the effective plastic strain, ε_y is the yield strain, σ_h is the hydrostatic stress, V_m is the molar volume, R is the gas constant, and T is the absolute temperature. We emphasise that k_{m} is a local variable, a function of the local ε^p and σ_h magnitudes.

Localised corrosion can be diffusion-controlled or activation-controlled. In the latter, the velocity of the moving pit boundary Γ follows Faraday's second law,

$$v_n = \boldsymbol{v} \cdot \mathbf{n} = \frac{i_a}{zF c_{\mathrm{solid}}} \tag{4}$$

where $\mathbf{n}$ is the unit normal vector to the pit interface, F is Faraday's constant, z is the average charge number and c_{solid} is the concentration of atoms in the metal. Then, the concentration of dissolved ions $c_{\mathrm{m}}(\mathbf{x}, t)$ at a point $\mathbf{x}$ in the interface can be calculated according to the Rankine–Hugoniot condition as,

$$\left[D \nabla c_{\mathrm{m}} + \left(c_{\mathrm{m}}(\mathbf{x}, t) - c_{\mathrm{solid}}\right) \boldsymbol{v}\right] \cdot \mathbf{n} = 0 \tag{5}$$

where D is the diffusion coefficient.

On the other hand, corrosion becomes diffusion controlled when the surface concentration reaches the saturation concentration c_{sat}, due to the accumulation of metal ions along the pit boundary. The pit interface velocity becomes then controlled by the diffusion of metal ions away from the pit boundary and the moving pit boundary velocity can be obtained by considering a saturated concentration in (5), such that

$$v_n = \frac{D\nabla c_{\text{m}} \cdot \mathbf{n}}{c_{\text{solid}} - c_{\text{sat}}} \tag{6}$$

Modelling the moving pit interface requires the application of both Robin (5) and Dirichlet ($c_{\text{m}} = c_{\text{sat}}$) boundary conditions for the activation-controlled and diffusion-controlled processes, respectively. Instead, we circumvent these complications by following the phase field paradigm proposed by Mai et al. (2016), approximating the interface evolution implicitly by solving for an auxiliary variable ϕ. As shown in Fig. 2, the phase field takes values of $\phi = 0$ for the electrolyte and $\phi = 1$ for the metal, varying smoothly between these two values along the interface Γ. Also, for consistency, a normalised concentration is defined as $c = c_{\text{m}}/c_{\text{solid}}$ (Mai et al., 2016). Thus, the normalised concentration c will equal 1 in the metal (solid) phase, and will approach 0 with increasing distance from the metal-electrolyte interface.

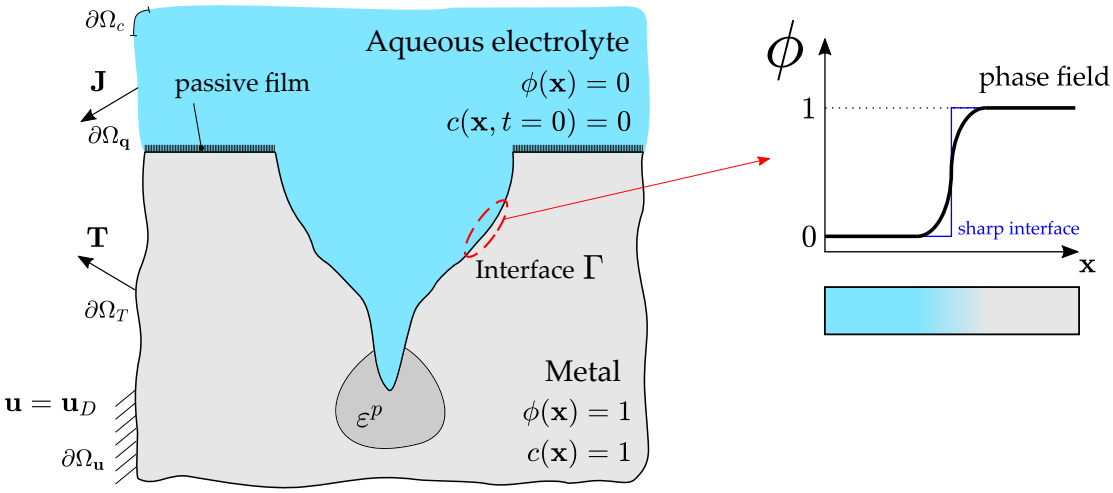

Figure 2: Schematic of the phase field approximation of the localised corrosion damage process, including the electrolyte phase ($\phi = 0$), the solid metal phase ($\phi = 1$), and the interface Γ at a time t.

In our current phase field method, material dissolution is governed by the interface kinetics coefficient L rather than the current density i_a. The magnitude of L can be considered to be a constant positive number (see, e.g., Mai et al., 2016). Here, we assume a time-dependent L instead, enriching the modelling capabilities by establishing a relation with our FRDR mechanistic interpretation and our definition of a mechanochemically-enhanced corrosion current density $i_a(t_i)$. Thus, from Eqs. (2)-(3) and assuming a linear relationship between L and i_a, the interface kinetics coefficient over a time interval t_i is defined as

$$L = \begin{cases} k_{\mathrm{m}}\left(\varepsilon^p, \sigma_h\right) L_0, & \text{if } 0 < t_i \leqslant t_0 \\ k_{\mathrm{m}}\left(\varepsilon^p, \sigma_h\right) L_0 \, \exp\left(-k\left(t_i - t_0\right)\right), & \text{if } t_0 < t_i \leqslant t_0 + t_f \end{cases} \tag{7}$$

Our phase field formulation can capture both pitting corrosion and stress corrosion cracking by coupling the displacement $\boldsymbol{u}$, the phase field order parameter ϕ, and the normalised metal ion concentration c in the electro-mechanical system. The theoretical formulation behind our model is described in *Appendix A*, while further details of the numerical implementation are given in *Appendix B*.

2. Abaqus UEL subroutine

The phase field model for corrosion is implemented by means of an Abaqus UEL subroutine which allows for user-defined computation of the element tangent stiffness matrices and the nodal force vectors. We consider isoparametric 2D quadrilateral elements (linear and quadratic) with 4 degrees of freedom per node, i.e. u_x, u_y, ϕ, and c, and four integration points. The extension to a three dimensional case is straightforward. Note that, following (Martínez-Pañeda et al., 2018), we use the temperature degree-of-freedom to model the concentration field. This will allow us to define initial conditions, run transient and steady-state analysis and impose different convergence criteria (if needed).

A number of quantities are stored as solution-dependent state variables `SVARS` to ease postprocessing and store history dependent variables. These are shown in Table 1. The stress variables refer to the undamaged stress

tensor $\boldsymbol{\sigma}_0$ but the hydrostatic stress refers to the damaged one:

$$\sigma_h = (h(\phi) + \kappa)\,\sigma_{h0} = \left(-2\phi^3 + 3\phi^2 + \kappa\right)\sigma_{h0} \tag{8}$$

where $\kappa = 1 \times 10^{-7}$ is a small positive parameter introduced to circumvent the complete degradation of the energy and ensure that the algebraic conditioning number remains well-posed.

The work hardening behaviour of the material is calculated by assuming an isotropic power law hardening behaviour, such that the flow stress σ and the effective plastic strain ε^p are related by,

$$\sigma = \sigma_y \left(1 + \frac{E\varepsilon^p}{\sigma_y}\right)^N \tag{9}$$

where E is Young's modulus, σ_y is the yield stress and N is the strain hardening exponent ($0 \leqslant N \leqslant 1$).

Variable	SVARS numbering
Axial stresses - σ_{11} , σ_{22} , σ_{33}	SVARS(1), SVARS(2), SVARS(3)
Shear stress - σ_{12}	SVARS(4)
Axial strains - ε_{11} , ε_{22} , ε_{33}	SVARS(5), SVARS(6), SVARS(7)
Shear strain - ε_{12}	SVARS(8)
Axial elastic strains - ε^e_{11} , ε^e_{22} , ε^e_{33}	SVARS(9), SVARS(10), SVARS(11)
Shear elastic strain - ε^e_{12}	SVARS(12)
Axial plastic strains - ε^p_{11} , ε^p_{22} , ε^p_{33}	SVARS(13), SVARS(14), SVARS(15)
Shear plastic strain - ε^p_{12}	SVARS(16)
Equivalent plastic strain - ε^p	SVARS(17)
Phase field - ϕ	SVARS(18)
Interface kinetics coefficient - L	SVARS(19)
Hydrostatic stress - σ_h	SVARS(20)
Equivalent plastic strain increment - $\Delta\varepsilon^p$	SVARS(21)
Concentration - c	SVARS(22)
Time period within the FRDR cycle - t_i	SVARS(23)
Effective plastic strain within the FRDR cycle - ε^p_i	SVARS(24)

Table 1: List of solution dependent state variables for the UEL.

The use of user element subroutines has the drawback that integration point variables cannot be visualized in Abaqus/Viewer. This limitation is intrinsic to the fact that the only information that Abaqus requests from the UEL subroutine are the stiffness matrix and the right-hand side nodal force vector - the magnitude of the stresses and the strains, as well as the choice of shape functions, is information that is not available as output. To overcome this limitation, we make use of an auxiliary dummy mesh consisting of standard Abaqus elements that resemble the user defined element in terms of number of nodes and integration points (i.e., CPE4 or CPE8R). The material response at each integration point in the auxiliary mesh is defined using a user material subroutine (UMAT), which enables the user to define the constitutive matrix and the stresses from the strain values. In this auxiliary mesh, the stress components and the constitutive matrix are made equal to zero (i.e., they have no influence in the solution of the global system). The data from our UEL that we want to observe in Abaqus/Viewer is stored in a Fortran module (`kvisual`), which allows transferring to the UMAT subroutine. In the UMAT the information is passed to the built-in array `STATEV` for each corresponding element and integration point. If SDV variables are requested as Field Output we would be able to visualize the results. Table 2 shows the equivalence between model variables and SDVs. In this cases, all the stress quantities correspond to the damaged stress tensor $\boldsymbol{\sigma}$.

2.1. Usage instructions

The first step is to create the model in Abaqus/CAE. The procedure is the same as with standard Abaqus models with the following subtleties:

- The material has to be defined as a user material with 24 solution-dependent variables. (General → Depvar: 24 & General → User Material - Mechanical Constants: 0). Additionally, since we are using the coupled mechanical-temperature step we need to define the density (General → Density) and the specific heat (Thermal → Specific Heat); both are irrelevant in our analysis and are therefore defined equal to 1.

- SDV, Solution dependent state variables, have to be requested as Field Output (as well as displacement, reaction forces and other relevant quantities). (Field Output Request - State/Field/User/Time: SDV, Solution dependent state variables)

Variable	SDVs numbering
Axial stresses - σ_{11} , σ_{22} , σ_{33}	SDV(1), SDV(2), SDV(3)
Shear stress - σ_{12}	SDV(4)
Axial strains - ε_{11} , ε_{22} , ε_{33}	SDV(5), SDV(6), SDV(7)
Shear strain - ε_{12}	SDV(8)
Axial elastic strains - ε^e_{11} , ε^e_{22} , ε^e_{33}	SDV(9), SDV(10), SDV(11)
Shear elastic strain - ε^e_{12}	SDV(12)
Axial plastic strains - ε^p_{11} , ε^p_{22} , ε^p_{33}	SDV(13), SDV(14), SDV(15)
Shear plastic strain - ε^p_{12}	SDV(16)
Equivalent plastic strain - ε^p	SDV(17)
Phase field - ϕ	SDV(18)
Interface kinetics coefficient - L	SDV(19)
Hydrostatic stress - σ_h	SDV(20)
Equivalent plastic strain increment - $\Delta\varepsilon^p$	SDV(21)
Concentration - c	SDV(22)
Time period within the FRDR cycle - t_i	SDV(23)
Effective plastic strain within the FRDR cycle - ε^p_i	SDV(24)

Table 2: List of solution dependent state variables.

- In the Step definition we select the coupled temperature-displacement option, as discussed before. Note that the time has a physical meaning. Also, note that, by default, the load is prescribed instantaneously with this Step type. One has to define and make use of amplitude functions accordingly to prescribe the boundary conditions; this is discussed below.

- The mesh has to be very refined in the expected SCC area. We recommend that the characteristic element size should be at least 5 times smaller than ℓ to resolve the SCC zone.

Once the model has been developed, we create a job and write the input file (Right click on the Job name and click "Write Input"). A few modifications have to be done to the input file to define the user element, the use of a code editor such as Notepad++ is recommended. First, we create the dummy visualization mesh. For this purpose we use the Matlab script VirtualMesh.m, which is part of the Abaqus2Matlab package (Papazafeiropoulos

et al., 2017). Running VirtualMesh.m on the same folder as the input file (Job-1.inp) will create a new file (VisualMesh.inp) with the element connectivity of the visualization mesh.

The first step is to replace the element type,

```
*Element, type=CPE8R
```

with the user element definition,

```
*User element, nodes=8, type=U1, properties=12, coordinates=2, var=96
1,2
1,3
1,11
*ELEMENT, TYPE=U1, ELSET=SOLID
```

where we have defined the number of nodes, the number of properties that will be defined in the input file, the number of coordinates (2D), and the number of `SVARS` (24 per integration point). Thus, in a 4-node element, the variable `U` contains the components: u_x^1, u_y^1, u_x^2, u_y^2, u_x^3, u_y^3, u_x^4, u_y^4, ϕ^1, ϕ^2, ϕ^3, ϕ^4, c^1, c^2, c^3 and ϕ^4. Accordingly, if one wishes to prescribe an initial corrosion region through the phase field parameter, then $\phi = 0$ and $c = 0$ should be enforced, using DOFs 3 and 11, respectively.

After the element connectivity list one inserts,

```
*UEL PROPERTY, ELSET=SOLID
190000, 0.3, 520, 0.067, 8.5e-4, 1.e-3, 4.8e-5, 33.3,
53.5, 0.0002, 3.e-3, 10.
*Element, type=CPE8R, elset=Visualization
```

and immediately afterwards the visualization connectivity list (i.e., the content of the file VisualMesh.inp created by the Matlab script). Here, we have defined the user element properties following Table 3. Throughout our model we employ SI (mm) units.

UEL PROPERTY	Description
PROPS(1)	E - Young's modulus [MPa]
PROPS(2)	ν - Poisson's ratio
PROPS(3)	σ_y - Yield stress [MPa] - see (9)
PROPS(4)	N - Strain hardening exponent - see (9)
PROPS(5)	D - Diffusion coefficient [mm^2/s] - see (5)
PROPS(6)	L_0 - Initial interface kinetics coefficient [mm^2/(N $\cdot$ s)] - see (A.28)
PROPS(7)	α - gradient energy coefficient - see (A.23)
PROPS(8)	w - Height of the double well potential - see (A.23)
PROPS(9)	A - Free energy density curvature [N/mm^2] - see (A.20)
PROPS(10)	k - Exponential term in the FRDR formulation - see (A.28)
PROPS(11)	ε_f - Strain required for film rupture - see (1)
PROPS(12)	t_0 - Time interval before new passive films formed [s] - see (1)

Table 3: List of user element properties.

Finally, note that, since we have defined our dummy connectivity list within the element set "Visualization", we need to modify the Section definition,

```
*Solid Section, elset=Set-1, material=Material-1
```

to change the name of the element set,

```
*Solid Section, elset=Visualization, material=Material-1
```

Additionally, one should note that a Fortran module has been defined in the first lines of the subroutine for visualization purposes. One has to be sure that the last dimension of the variable `UserVar` is larger than the total number of elements.

2.2. Example: SCC from a semi-ellipse pit

We implement a rectangular stainless steel plate with an initial semi-ellipse shaped pit to showcase the impact of mechanical stress and the repassivation effects on SCC process. The geometric setup, dimensions and boundary conditions are given in Fig. 3. The corrosion parameters in this study are listed in Table 4 and the mechanical parameters are defined as: $E = 190\,\text{GPa}$, $\nu = 0.3$, $\sigma_\text{Y} = 520\,\text{MPa}$ and $N = 0.067$ according to Lu et al. (2016).

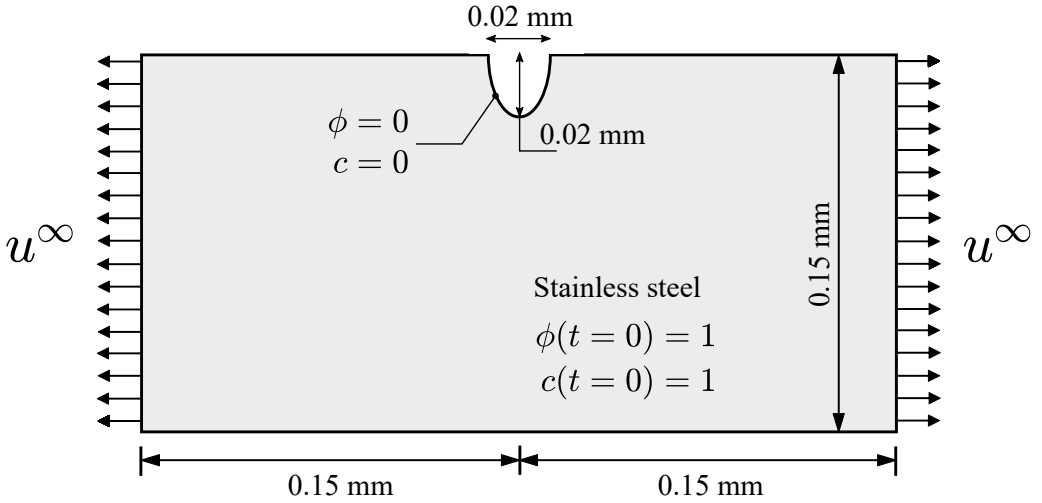

Figure 3: Geometric setup and initial/boundary conditions of the parametric study.

Parameter	**Value**	**Unit**
Interface energy γ	0.01	N/mm
Phase field length scale l (Appendix C.2)	0.005	mm
Diffusion coefficient D	8.5×10^{-4}	mm^2/s
Interface kinetics coefficient L_0	0.001	$\mathrm{mm}^2/(\mathrm{N} \cdot \mathrm{s})$
Free energy density curvature A	53.5	$\mathrm{N/mm}^2$
Average concentration of metal c_{solid}	143	mol/L
Average saturation concentration c_{sat}	5.1	mol/L

Table 4: Corrosion parameters used in this study.

We investigate the influence of repassivation and assign an initial displacement of $u = 0.1\,\mu$m, which is held constant throughout the analysis. The film rupture-dissolution-repassivation (FRDR) process is captured using $\varepsilon_f = 3 \times 10^{-3}$, $t_0 = 10\,$s and three different value of the parameter characterising the corrosion sensitivity to the stability of the passive film: $k = 0.0002$, $k = 0.0005$, and $k = 0.001$. It should be emphasised that the boundary conditions are implemented over four steps, using amplitudes. The goal is to allow the solution to stabilise and facilitate convergence. Thus, in the first step (`Step-1`) we initialise the system by prescribing $\phi = c = 1$ everywhere. The second step (`Step-2`) removes the constraints over ϕ and c to allow the

solution to evolve freely according to the governing equations. We then prescribe the remote displacement in `Step-3`, this is done instantaneously and we then allow the solution to stabilise with a constant displacement. Finally, in `Step-4` we prescribe $\phi = c = 0$ at the interface. Rather than doing this abruptly, we use an amplitude to enforce this condition over a short time period (0.005 s), such that the nodes at the interface vary linearly from 1 to 0, and then hold the boundary condition fixed at $\phi = c = 0$, allowing the corrosion process to evolve. There are likely to be simpler ways of prescribing this set of boundary conditions, but we emphasise that doing so in a staggered manner and with smooth transitions assists with convergence. Other issues related to convergence and the numerical model are given in Appendix C.

Fig. 4 shows the related SCC evolution laws when the corrosion time $t = 900\,\mathrm{s}$. As can be seen, the impact of k in the SCC morphology is evident: higher k values accelerate the SCC defect growth rate in the pit base relative to corrosion rates at the pit mouth, sharpening the pit and triggering a pit-to-crack transition. Note that, to capture precisely the SCC evolution shown in Fig. 4c, the model should be edited to extend the size of the area where the mesh has been refined. Corrosion rates at the tip of the SCC defect are exacerbated as the defect sharpens and plasticity localises; the protective film is weaker in areas of high mechanical straining - see Eq. (1). The length of the SCC region is shown in Fig. 5 as a function of the film stability parameter k, including the case where no film is present ($k = 0$). The results reveal that by introducing the repassivation process, the length of the SCC region drops slightly at an early stage, which is in accordance with the fact that repassivation will restrain the SCC process by decreasing the value of interface kinetics coefficient. After a certain time, the size of the SCC region grows faster with increasing k as film rupture occurs and the magnitude of the equivalent plastic strain increases as the defect sharpens, augmenting the interface kinetics coefficient - see Eq. (7).

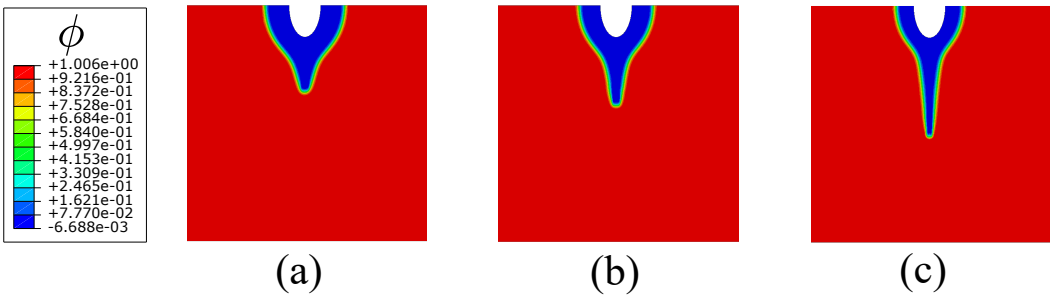

Figure 4: SCC from a semi-elliptical pit. Contours of the phase field after $t = 900$ s for a remote displacement of $u^{\infty} = 0.1$ μm and three selected values of the film stability parameter: (a) $k = 2 \times 10^{-4}$, (b) $k = 5 \times 10^{-4}$, and (c) $k = 1 \times 10^{-3}$.

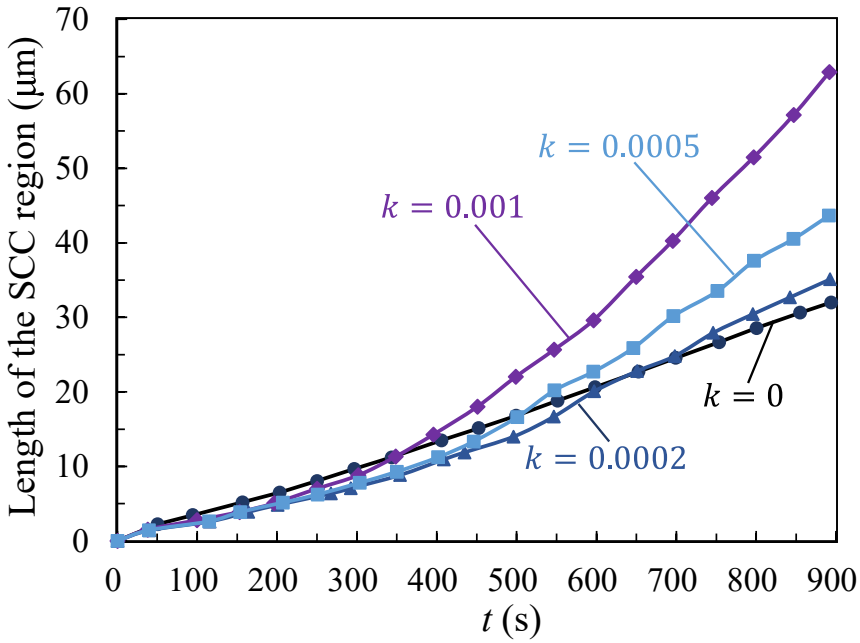

Figure 5: SCC from a semi-elliptical pit. Length of the SCC region as a function of time for a remote displacement of $u^{\infty} = 0.1$ μm and four selected values of the film stability parameter.

3. Concluding remarks

We have provided a finite element implementation of the phase field model for corrosion damage developed by (Cui et al., 2021). The present document

provides extensive details of the accompanying code (PhaseFieldSCC.for), which can be downloaded from www.empaneda.com/codes. Do not hesitate to contact us if questions that have not been clarified here arise.

4. Acknowledgements

C. Cui acknowledges financial support from National Natural Science Foundation of China under grant No. 51878493. E. Martínez-Pañeda acknowledges financial support from the EPSRC (grants EP/R010161/1 and EP/R017727/1) and from the Royal Commission for the 1851 Exhibition (RF496/2018).

Appendix A. Theory

Appendix A.1. Principle of virtual work and balance equations

Our theory deals with the coupled behaviour of two systems, one mechanical and one electrochemical one, see Fig. 2. These two systems are coupled by the following physical phenomena: (i) the pit evolution process is accelerated by mechanics, as presented in Eqs. (2) and (3); and (ii) the dissolution of metals leads to a redistribution of mechanical stress. With respect to the mechanical contributions, the outer surface of the body is decomposed into a part $\partial\Omega_u$, where the displacement can be prescribed by Dirichlet-type boundary conditions, and a part $\partial\Omega_T$, where a traction $\boldsymbol{T}$ can be prescribed by Neumann-type boundary conditions. As for the electrochemical part, the external surface consists on two parts: $\partial\Omega_q$ where the flux $\boldsymbol{J}$ is known (Neumman-type boundary conditions), and $\partial\Omega_c$, where the concentration is prescribed (Dirichlet-type boundary conditions). Accordingly, a concentration flux entering the body across $\partial\Omega_q$ can be defined as $q = \boldsymbol{J}\cdot\boldsymbol{n}$. Solute diffusion is driven by the chemical potential μ, as constitutively characterised below. We follow Duda et al. (2018) in defining a scalar field η to determine the kinematics of composition changes, such that

$$\dot{\eta} = \mu \quad \text{and} \quad \eta(\mathbf{x},t) = \int_0^t \mu(\mathbf{x},t)\,\mathrm{d}t \tag{A.1}$$

Thus, from a kinematic viewpoint, the domain Ω can be described by the displacement $\boldsymbol{u}$, phase parameter ϕ and chemical displacement η. We denote

the set of virtual fields as ($\delta\boldsymbol{u}$, $\delta\phi$, $\delta\eta$) and proceed to introduce the principle of virtual work for the coupled systems as,

$$\begin{aligned}\int_\Omega \left\{ \boldsymbol{\sigma} : \delta\boldsymbol{\varepsilon} + \frac{1}{L}\frac{d\phi}{dt}\delta\phi + \omega\delta\phi + \boldsymbol{\zeta}\cdot\nabla\delta\phi - \frac{dc}{dt}c_{\text{solid}}\,\delta\eta + \boldsymbol{J}\cdot\nabla\delta\eta \right\} \mathrm{d}V \\ = \int_{\partial\Omega} \left\{ f\delta\phi + q\delta\eta + \boldsymbol{T}\cdot\delta\boldsymbol{u} \right\} \mathrm{d}S\end{aligned} \tag{A.2}$$

where $\boldsymbol{\varepsilon}$ is the strain tensor, which is computed from the displacement field in the usual manner $\boldsymbol{\varepsilon} = \mathrm{sym}\nabla\boldsymbol{u}$ and additively decomposes into an elastic part $\boldsymbol{\varepsilon}^e$ and a plastic part $\boldsymbol{\varepsilon}^p$. Also, we use L to denote the interface kinetics coefficient, f is the phase field microtraction and ω and $\boldsymbol{\zeta}$ are the microstress quantities work conjugate to the phase field ϕ and the phase field gradient $\nabla\phi$, respectively. Operating, and making use of Gauss' divergence theorem:

$$\begin{aligned}\int_\Omega \left\{ (\nabla\cdot\boldsymbol{\sigma})\cdot\delta\boldsymbol{u} + \left(\nabla\cdot\boldsymbol{\zeta} - \omega - \frac{1}{L}\frac{d\phi}{dt}\right)\delta\phi + \left(\nabla\cdot\boldsymbol{J} + \frac{dc}{dt}c_{\text{solid}}\right)\delta\eta \right\} \mathrm{d}V \\ = \int_{\partial\Omega} \left\{ (\boldsymbol{\sigma}\boldsymbol{n} - \boldsymbol{T})\cdot\delta\boldsymbol{u} + (\boldsymbol{\zeta}\cdot\boldsymbol{n} - f)\,\delta\phi + (\boldsymbol{J}\cdot\boldsymbol{n} - q)\,\delta\eta \right\} \mathrm{d}S\end{aligned} \tag{A.3}$$

Finally, considering that the left-hand side of Eq. (A.3) must vanish for arbitrary variations, the equilibrium equations in Ω for each primary kinematic variable are obtained as

$$\begin{aligned}\nabla\cdot\boldsymbol{\sigma} &= \boldsymbol{0} \\ (\nabla\cdot\boldsymbol{\zeta} - \omega) - \frac{1}{L}\frac{d\phi}{dt} &= 0 \\ \frac{dc}{dt}c_{\text{solid}} + \nabla\cdot\boldsymbol{J} &= 0\end{aligned} \tag{A.4}$$

with the right-hand side of Eq. (A.3) providing the corresponding set of boundary conditions on $\partial\Omega$,

$$\begin{aligned}\boldsymbol{T} &= \boldsymbol{\sigma}\cdot\boldsymbol{n} \\ f &= \boldsymbol{\zeta}\cdot\boldsymbol{n} \\ q &= \boldsymbol{J}\cdot\boldsymbol{n}\end{aligned} \tag{A.5}$$

Appendix A.2. Energy imbalance

The first two laws of thermodynamics for a continuum body within a dynamical process of specific internal energy $\mathscr{E}$ and specific entropy Λ read

(Gurtin et al., 2010),

$$\begin{aligned} \frac{d}{dt}\int_\Omega \mathscr{E}\,\mathrm{d}V &= \dot{W}_e\left(\Omega\right) - \int_{\partial\Omega} \boldsymbol{Q}\cdot\boldsymbol{n}\,\mathrm{d}S + \int_\Omega Q\,\mathrm{d}V \\ \frac{d}{dt}\int_\Omega \Lambda\,\mathrm{d}V &\geqslant -\int_{\partial\Omega}\frac{\boldsymbol{Q}}{T}\cdot\boldsymbol{n}\,\mathrm{d}S + \int_\Omega \frac{Q}{T}\,\mathrm{d}V \end{aligned} \tag{A.6}$$

where $\dot{W}_e$ is the power of external work, $\boldsymbol{Q}$ is the heat flux and Q is the heat absorption. The resulting Clausius-Duhem inequality must be fulfilled by the free energies associated with both systems, mechanical ψ^M and electrochemical ψ^E. Thus, the energy imbalances associated with the mechanical and electrochemical systems can be obtained by assuming an isothermal process ($T = T_0$) and replacing the virtual fields ($\delta\boldsymbol{u}$, $\delta\phi$, $\delta\eta$) by the realizable velocity fields $\left(\dot{\boldsymbol{u}},\, \dot{\phi},\, \mu\right)$ in Eq. (A.2),

$$\frac{d}{dt}\int_\Omega \psi^M\,\mathrm{d}V \leqslant \int_{\partial\Omega}\boldsymbol{T}\cdot\dot{\boldsymbol{u}}\,\mathrm{d}S \tag{A.7}$$

$$\frac{d}{dt}\int_\Omega \psi^E\,\mathrm{d}V \leqslant \int_{\partial\Omega}\left(f\dot{\phi} + q\mu\right)\,\mathrm{d}S \tag{A.8}$$

Employing the divergence theorem and recalling the local balance equations (A.4)-(A.5), we find the equivalent point-wise version of Eqs. (A.7)-(A.8) as,

$$\dot{\psi}^M - \boldsymbol{\sigma} : \dot{\boldsymbol{\varepsilon}} \leqslant 0 \tag{A.9}$$

$$\dot{\psi}^E - \frac{1}{L}\ddot{\phi} - \omega\dot{\phi} - \boldsymbol{\zeta}\cdot\nabla\dot{\phi} + \mu\dot{c}\,c_{\text{solid}} - \boldsymbol{J}\cdot\nabla\mu \leqslant 0 \tag{A.10}$$

Appendix A.3. Constitutive theory

We proceed to define the functional form of free energy of each system and subsequently derive a set of thermodynamically consistent relations.

Appendix A.3.1. Constitutive prescriptions for the mechanical problem

The mechanical behaviour of the solid is characterised by von Mises J2 plasticity theory. The extension to strain gradient plasticity (Martínez-Pañeda and Fleck, 2019; Martínez-Pañeda et al., 2019), of particular importance when dealing with sharp pits and cracks, will be addressed in future

works. Accordingly, the mechanical free energy is decomposed into elastic ψ^e and plastic ψ^p components, both of which are degraded by the phase field,

$$\psi^M = h(\phi)\left(\psi^e + \psi^p\right) \tag{A.11}$$

Here, $h(\phi)$ is the degradation function characterising the transition from the undissolved solid ($\phi = 1$) to the electrolyte phase ($\phi = 0$). The definition of $h(\phi)$ must satisfy the conditions $h(\phi = 0) = 0$ and $h(\phi = 1) = 1$; here,

$$h\left(\phi\right) = -2\phi^3 + 3\phi^2 \tag{A.12}$$

Consistent with (A.9), the Cauchy stress tensor is defined as $\boldsymbol{\sigma} = \partial_{\boldsymbol{\varepsilon}}\psi^M$ and we denote $\boldsymbol{\sigma}_0$ as the Cauchy stress tensor for the undissolved solid. Thus, accounting for the influence of the phase field and using $\boldsymbol{\sigma}_0$, the mechanical force balance (A.4a) can be reformulated as,

$$\nabla \cdot \left[\left(h\left(\phi\right) + \kappa\right)\boldsymbol{\sigma_0}\right] = \mathbf{0} \tag{A.13}$$

where κ is a small positive parameter introduced to circumvent the complete degradation of the energy and ensure that the algebraic conditioning number remains well-posed. We adopt $\kappa = 1 \times 10^{-7}$ throughout this work.

The elastic strain energy density is defined as a function of the elastic strains $\boldsymbol{\varepsilon}^e$ and the linear elastic stiffness matrix $\boldsymbol{C}_0$ in the usual manner,

$$\psi^e\left(\boldsymbol{\varepsilon}^e\right) = \frac{1}{2}\left(\boldsymbol{\varepsilon}^e\right)^T : \boldsymbol{C}_0 : \boldsymbol{\varepsilon}^e \tag{A.14}$$

While the plastic strain energy density is incrementally computed from the plastic strain tensor $\boldsymbol{\varepsilon}^p$ and the Cauchy stress tensor for the undissolved solid $\boldsymbol{\sigma}_0$ as,

$$\psi^p = \int_0^t \boldsymbol{\sigma}_0 : \dot{\boldsymbol{\varepsilon}}^p \, \mathrm{d}t \tag{A.15}$$

Appendix A.3.2. Constitutive prescriptions for the electrochemical problem

In the localised corrosion system described in Section 1, the electrochemical free energy density ψ^E can be decomposed into its chemical and interface counterparts,

$$\psi^E = \psi^{ch} + \psi^i \tag{A.16}$$

The chemical free energy density ψ^{ch} can be further decomposed into the energy associated with material composition and a double-well potential energy (Mai et al., 2016), such that

$$\psi^{ch} = h\left(\phi\right)\psi_{\mathrm{S}}^{ch} + \left(1 - h(\phi)\right)\psi_{\mathrm{L}}^{ch} + wg\left(\phi\right) \tag{A.17}$$

where the parameter w is the height of the double well potential $g\left(\phi\right) = \phi^2(1-\phi)^2$, and ψ_{S}^{ch} and ψ_{L}^{ch} denote the chemical free energy density terms associated with the solid and liquid phases, respectively. These latter two terms are defined following the KKS model (Kim et al., 1999), which assumes that each material point is a mixture of both solid and liquid phases with different concentrations but similar chemical potentials. Following this assumption, one reaches the following balances

$$c = h\left(\phi\right)c_{\mathrm{S}} + \left[1 - h\left(\phi\right)\right]c_{\mathrm{L}} \tag{A.18}$$

$$\frac{\partial\psi_{\mathrm{S}}^{ch}\left(c_{\mathrm{S}}\right)}{\partial c_{\mathrm{S}}} = \frac{\partial\psi_{\mathrm{L}}^{ch}\left(c_{\mathrm{L}}\right)}{\partial c_{\mathrm{L}}} \tag{A.19}$$

where c_{S} and c_{L} are the normalized concentrations of the co-existing solid and liquid phases, respectively. Defining a free energy density curvature A, assumed to be similar for the solid and liquid phases, and restricting our attention to dilute solutions, we reach the following definitions for each component of the chemical free energy density,

$$\psi_{\mathrm{S}}^{ch} = A(c_{\mathrm{S}} - c_{\mathrm{Se}})^2 \quad \text{and} \quad \psi_{\mathrm{L}}^{ch} = A(c_{\mathrm{L}} - c_{\mathrm{Le}})^2 \tag{A.20}$$

where $c_{\mathrm{Se}} = c_{\mathrm{solid}}/c_{\mathrm{solid}} = 1$ and $c_{\mathrm{Le}} = c_{\mathrm{sat}}/c_{\mathrm{solid}}$ are the normalised *equilibrium* concentrations for the solid and liquid phases. Combining Eqs. (A.17)-(A.20) renders,

$$\psi^{ch} = A\left[c - h(\phi)(c_{\mathrm{Se}} - c_{\mathrm{Le}}) - c_{\mathrm{Le}}\right]^2 + w\phi^2\left(1-\phi\right)^2 \tag{A.21}$$

On the other hand, the interface free energy density ψ_i is defined as a function of the gradient of the phase field variable as:

$$\psi^{i} = \frac{\alpha}{2}|\nabla\phi|^2 \tag{A.22}$$

where α is the gradient energy coefficient. In the free energy density definitions (A.21)-(A.22), the parameters α and w govern the interface energy γ and its thickness l as:

$$\gamma = \frac{\sqrt{\alpha w}}{4} \quad \text{and} \quad l = a^*\sqrt{\frac{2\alpha}{w}} \tag{A.23}$$

where $a^* = 2.94$ is a constant parameter corresponding to the definition of the interface region $0.05 < \phi < 0.95$ (Abubakar et al., 2015).

Finally, the constitutive relations for the associated stress quantities can be readily obtained by fulfilling the free energy imbalance (A.10), which implies

$$-\frac{1}{L}\ddot{\phi} + \left(\frac{\partial \psi^E}{\partial \phi} - \omega\right)\dot{\phi} + \left(\frac{\partial \psi^E}{\partial \nabla \phi} - \boldsymbol{\zeta}\right) \cdot \nabla \dot{\phi} + \left(\frac{\partial \psi^E}{\partial c} + \mu c_{\text{solid}}\right)\dot{c} - \boldsymbol{J} \cdot \nabla \mu \leqslant 0 \tag{A.24}$$

Thus, the scalar microstress ω, work conjugate to the phase field ϕ, is given by

$$\omega = \frac{\partial \psi^E}{\partial \phi} = -2A\left[c - h(\phi)(c_{\text{Se}} - c_{\text{Le}}) - c_{\text{Le}}\right](c_{\text{Se}} - c_{\text{Le}})h'(\phi) + wg'(\phi) \tag{A.25}$$

while the vector microstress $\boldsymbol{\zeta}$, work conjugate to the phase field gradient, reads

$$\boldsymbol{\zeta} = \frac{\partial \psi^E}{\partial \nabla \phi} = \alpha \nabla \phi \tag{A.26}$$

Inserting these constitutive relations (A.25)-(A.26) into the phase field balance (A.4b) renders the so-called Allen-Cahn equation:

$$\frac{d\phi}{dt} + L\left(\frac{\partial \psi^E}{\partial \phi} - \alpha \nabla^2 \phi\right) = 0 \tag{A.27}$$

Eq. (A.27) shows that material dissolution is governed by the interface kinetics coefficient L. The magnitude of L can be considered to be a constant positive number (see, e.g., Mai et al., 2016). Here, we assume a time-dependent L instead, enriching the modelling capabilities by establishing a relation with our FRDR mechanistic interpretation and our definition of a mechanochemically-enhanced corrosion current density $i_a(t_i)$. Thus, from Eqs. (2)-(3) and assuming a linear relationship between L and i_a, the interface kinetics coefficient over a time interval t_i is defined as

$$L = \begin{cases} k_{\text{m}}\left(\varepsilon^p, \sigma_h\right) L_0, & \text{if } 0 < t_i \leqslant t_0 \\ k_{\text{m}}\left(\varepsilon^p, \sigma_h\right) L_0 \exp\left(-k\left(t_i - t_0\right)\right), & \text{if } t_0 < t_i \leqslant t_0 + t_f \end{cases} \tag{A.28}$$

The material dissolution process (pitting and cracking) can be either activation-controlled or diffusion-controlled and the constitutive choices for the mass transport process are obtained as follows. First, the chemical potential is given by,

$$\mu = -\frac{1}{c_{\text{solid}}}\frac{\partial \psi^E}{\partial c} = -\frac{2A}{c_{\text{solid}}}\left((c - h(\phi)(c_{\text{Se}} - c_{\text{Le}}) - c_{\text{Le}})\right) \tag{A.29}$$

Secondly, the flux $\boldsymbol{J}$ can be determined following a Fick law-type relation as,

$$\boldsymbol{J} = \frac{D}{2A}\cdot c_{\text{solid}}\cdot c_{\text{solid}}\cdot \nabla\mu = -c_{\text{solid}}\cdot D\nabla\left((c - h(\phi)(c_{\text{Se}} - c_{\text{Le}}) - c_{\text{Le}})\right) \tag{A.30}$$

Substituting Eqs. (A.29)-(A.30) into the mass transport balance Eq. (A.4c), the following field equation is obtained

$$\frac{dc}{dt} - \nabla\cdot D\nabla\left((c - h(\phi)(c_{\text{Se}} - c_{\text{Le}}) - c_{\text{Le}})\right) = 0 \tag{A.31}$$

which is an extension of Fick's second law such that diffusion of metal ions only takes place along the interface and in the electrolyte.

Appendix B. Numerical implementation

The finite element method is used to discretise and solve the coupled electro-chemo-mechanical problem. First, we formulate the weak form of the governing equations for the displacement (A.13), phase field (A.27), and concentration (A.31) problems, respectively. Thus,

$$\int_\Omega \left(h(\phi) + \kappa\right)\boldsymbol{\sigma}_0\delta\boldsymbol{\varepsilon}\,\mathrm{d}V - \int_{\partial\Omega}\boldsymbol{T}\cdot\delta\boldsymbol{u}\,\mathrm{d}S = 0 \tag{B.1}$$

$$\int_\Omega \frac{\partial\phi}{\partial t}\delta\phi\,\mathrm{d}V + L\int_\Omega \frac{\partial\psi^E}{\partial\phi}\delta\phi\,\mathrm{d}V + L\int_\Omega \alpha\nabla\phi\nabla\delta\phi\,\mathrm{d}V = 0 \tag{B.2}$$

$$\int_\Omega \frac{\partial c}{\partial t}\delta c\,\mathrm{d}V + D\int_\Omega \nabla\left[c - h(\phi)(c_{\text{Se}} - c_{\text{Le}}) - c_{\text{Le}}\right]\cdot\nabla\delta c\,\mathrm{d}V = 0 \tag{B.3}$$

Using Voigt notation, the nodal variables for the displacement field $\hat{\mathbf{u}}$, the phase field $\hat{\phi}$ and the normalised concentration $\hat{c}$ are interpolated as:

$$\boldsymbol{u} = \sum_{i=1}^{m}\mathbf{N}_i^{\mathbf{u}}\hat{\boldsymbol{u}}_i, \quad \phi = \sum_{i=1}^{m}N_i\hat{\phi}_i, \quad c = \sum_{i=1}^{m}N_i\hat{c}_i \tag{B.4}$$

where N_i denotes the shape function associated with node i, for a total number of nodes m. Here, $\mathbf{N}_i^{\mathbf{u}}$ is a diagonal interpolation matrix with the nodal shape functions N_i as components. Similarly, using the standard strain-displacement $\boldsymbol{B}$ matrices, the associated gradient quantities are discretised as:

$$\boldsymbol{\varepsilon} = \sum_{i=1}^{m} \mathbf{B}_i^{\mathbf{u}} \hat{\boldsymbol{u}}_i, \quad \nabla\phi = \sum_{i=1}^{m} \mathbf{B}_i \hat{\phi}_i, \quad \nabla c = \sum_{i=1}^{m} \mathbf{B}_i \hat{c}_i \tag{B.5}$$

Then, the weak form balances (B.1)-(B.3) are discretised in time and space, such that the resulting discrete equations of the balances for the displacement, phase field and concentration can be expressed as the following residuals:

$$\boldsymbol{r}_{i,\boldsymbol{u}}^{n+1} = \int_\Omega \left(h(\phi^{n+1}) + \kappa\right) (\mathbf{B}_i^{\mathbf{u}})^T \boldsymbol{\sigma}_0 \,\mathrm{d}V - \int_{\partial\Omega} (\mathbf{N}_i^{\mathbf{u}})^T \boldsymbol{T} \,\mathrm{d}S \tag{B.6}$$

$$r_{i,\phi}^{n+1} = \int_\Omega \frac{\phi^{n+1} - \phi^n}{\mathrm{d}t} N_i \,\mathrm{d}V + L \int_\Omega \frac{\partial \psi^E}{\partial \phi^{n+1}} N_i \,\mathrm{d}V + L \int_\Omega \alpha \mathbf{B}_i{}^T \nabla\phi^{n+1} \,\mathrm{d}V \tag{B.7}$$

$$r_{i,c}^{n+1} = \int_\Omega \frac{c^{n+1} - c^n}{\mathrm{d}t} N_i \,\mathrm{d}V + D \int_\Omega \mathbf{B}_i{}^T \left[\nabla c^{n+1} - h'(\phi^{n+1})(c_{\mathrm{Se}} - c_{\mathrm{Le}}) \nabla\phi^{n+1}\right] \,\mathrm{d}V \tag{B.8}$$

where $()^{n+1}$ denotes the $(n+1)$ time step and $\mathrm{d}t$ is the time increment. Subsequently, the tangent stiffness matrices are calculated as:

$$\mathbf{K}_{ij,\boldsymbol{u}}^{n+1} = \int_\Omega \left(h(\phi^{n+1}) + \kappa\right) (\mathbf{B}_i^{\mathbf{u}})^T \boldsymbol{C_{ep}} \mathbf{B}_j^{\mathbf{u}} \,\mathrm{d}V \tag{B.9}$$

$$\mathbf{K}_{ij,\phi}^{n+1} = \int_\Omega \frac{N_i N_j}{\mathrm{d}t} \,\mathrm{d}V + L \int_\Omega \frac{\partial^2 \psi^E}{\partial \phi^2} N_i N_j \,\mathrm{d}V + L \int_\Omega \alpha \mathbf{B}_i{}^T \mathbf{B}_j \,\mathrm{d}V \tag{B.10}$$

$$\mathbf{K}_{ij,c}^{n+1} = \int_\Omega \frac{N_i N_j}{\mathrm{d}t} \,\mathrm{d}V + D \int_\Omega \mathbf{B}_i{}^T \mathbf{B}_j \,\mathrm{d}V \tag{B.11}$$

where $\boldsymbol{C_{ep}}$ is the elastic-plastic consistent material Jacobian.

Finally, the linearized finite element system can be expressed as:

$$\begin{bmatrix} \mathbf{K}_{\boldsymbol{u}} & \mathbf{0} & \mathbf{0} \\ \mathbf{0} & \mathbf{K}_\phi & \mathbf{0} \\ \mathbf{0} & \mathbf{0} & \mathbf{K}_c \end{bmatrix} \begin{bmatrix} \boldsymbol{u} \\ \boldsymbol{\phi} \\ \boldsymbol{c} \end{bmatrix} = \begin{bmatrix} \boldsymbol{r}_{\boldsymbol{u}} \\ \boldsymbol{r}_\phi \\ \boldsymbol{r}_c \end{bmatrix} \tag{B.12}$$

Appendix C. Formulation details

In the input file attached, dealing with a plane strain problem, each element contains four degree of freedoms: $\boldsymbol{u}(u_x, u_y), \phi$, and c. As discussed in Appendix A, these DOFs are controlled by three governing equations, we write their strong forms again to clarify some details in our formulation.

$$\nabla \cdot \left[\left(h\left(\phi\right) + \kappa \right) \boldsymbol{\sigma_0} \right] = \mathbf{0} \tag{C.1}$$

$$\frac{1}{L}\frac{d\phi}{dt} - 2A\left[c - h(\phi)(c_{\mathrm{Se}} - c_{\mathrm{Le}}) - c_{\mathrm{Le}}\right](c_{\mathrm{Se}} - c_{\mathrm{Le}})h'(\phi) + wg'(\phi) - \alpha\nabla^2\phi = 0 \tag{C.2}$$

$$\frac{dc}{dt} - \nabla \cdot D\nabla\left((c - h(\phi)(c_{\mathrm{Se}} - c_{\mathrm{Le}}) - c_{\mathrm{Le}})\right) = 0 \tag{C.3}$$

Appendix C.1. Activation-controlled versus diffusion-controlled corrosion

As we discussed in Section 1, pitting corrosion can be either activation-controlled or diffusion-controlled. As indicated in (C.2) and (C.3), activation is mainly governed by the interface kinetics coefficient L while diffusion is mainly governed by the coefficient D. Obviously, increasing L increases the metal dissolution speed. However, if L is sufficiently high, corrosion process would be diffusion-controlled and limited by the value of diffusion coefficient D. We depicted this competition relation in our paper (Cui et al., 2021) through the well-known pencil electrode test, see Section 4.1 in the journal article.

In this regard, it is worth emphasising that we incorporate the mechanochemical interactions and the FRDR process through a time-dependent interface kinetics coefficient $L = L(t)$, as presented in (7). Thus, these process can trigger a transition from activation-controlled corrosion to diffusion-controlled corrosion, and this is a natural byproduct of our model.

Appendix C.2. Interface thickness l

The interface thickness, as characterised by the parameter l, is not given explicitly in the governing equations. Instead, the magnitude of l is governed by the height of double-well potential w and the gradient of the phase field variable α, as formulated in (A.23). One can readily see that larger values of l would translate in a smaller value of w (for a fixed α) and a larger value of α (for a fixed w). Thus, results are sensitive to the choice of ℓ; the interface thickness is a material parameter that should be determined experimentally. At least 4-5 elements should be used to resolve the interface thickness.

Appendix C.3. Convergence condition

Some notes on convergence follow. First, note convergence might be facilitated if a Forward Euler approach is used for the couplings, as opposed to a Backward Euler-type approach. Thus, convergence could be facilitated if the hydrostatic stress σ_h and the effective plastic strain ε^p values used in the phase field corrosion evolution law, see (3), are taken from the previous increment. However, this comes at the cost of losing the unconditionally stability property; for results to be accurate, the time increment should be kept small. Also, in our experience differences are small in terms of convergence; thus, We have computed σ_h using a backward Euler approach.

Finally, we emphasise that using a larger value of L requires a smaller time increment to achieve convergence. Given the impact of mechanical fields on L in our model, we suggest giving flexibility to the solution system using an automatic time incrementation scheme (as it is the case in the input file provided).

References

Abubakar, A.A., Akhtar, S.S., Arif, A.F.M., 2015. Phase field modeling of V2O5 hot corrosion kinetics in thermal barrier coatings. Computational Materials Science 99, 105–116.

Cui, C., Ma, R., Martínez-Pañeda, E., 2021. A phase field formulation for dissolution-driven stress corrosion cracking. Journal of the Mechanics and Physics of Solids 147, 104254.

Dai, H., Shi, S., Guo, C., Chen, X., 2020. Pits formation and stress corrosion cracking behavior of Q345R in hydrofluoric acid. Corrosion Science 166, 108443.

Duda, F.P., Ciarbonetti, A., Toro, S., Huespe, A.E., 2018. A phase-field model for solute-assisted brittle fracture in elastic-plastic solids. International Journal of Plasticity 102, 16–40.

Gurtin, M.E., Fried, E., Anand, L., 2010. The Mechanics and Thermodynamics of continua. Cambridge University Press, Cambridge, UK.

Gutman, E.M., 1998. Mechanochemistry of materials. Cambridge International Science Publishing, Cambridge, UK.

Gutman, E.M., 2007. An inconsistency in "film rupture model" of stress corrosion cracking. Corrosion Science 49, 2289–2302.

Jivkov, A.P., 2004. Strain-induced passivity breakdown in corrosion crack initiation. Theoretical and Applied Fracture Mechanics 42, 43–52.

Kim, S.G., Kim, W.T., Suzuki, T., 1999. Phase-field model for binary alloys. Physical Review E - Statistical Physics, Plasmas, Fluids, and Related Interdisciplinary Topics 60, 7186–7197.

Kristensen, P.K., Martínez-Pañeda, E., 2020. Phase field fracture modelling using quasi-Newton methods and a new adaptive step scheme. Theoretical and Applied Fracture Mechanics 107, 102446.

Lu, J., Sun, W., Becker, A., 2016. Material characterisation and finite element modelling of cyclic plasticity behaviour for 304 stainless steel using a crystal plasticity model. International Journal of Mechanical Sciences 105, 315–329.

Macdonald, D.D., 1999. Passivity - the key to our metals-based civilization. Pure and Applied Chemistry 71, 951–978.

Mai, W., Soghrati, S., Buchheit, R.G., 2016. A phase field model for simulating the pitting corrosion. Corrosion Science 110, 157–166.

Martínez-Pañeda, E., Deshpande, V.S., Niordson, C.F., Fleck, N.A., 2019. The role of plastic strain gradients in the crack growth resistance of metals. Journal of the Mechanics and Physics of Solids 126, 136–150.

Martínez-Pañeda, E., Fleck, N.A., 2019. Mode I crack tip fields: Strain gradient plasticity theory versus J2 flow theory. European Journal of Mechanics - A/Solids 75, 381–388.

Martínez-Pañeda, E., Golahmar, A., Niordson, C.F., 2018. A phase field formulation for hydrogen assisted cracking. Computer Methods in Applied Mechanics and Engineering 342, 742–761.

Papazafeiropoulos, G., Muñiz-Calvente, M., Martínez-Pañeda, E., 2017. Abaqus2Matlab: A suitable tool for finite element post-processing. Advances in Engineering Software 105, 9–16.

Parkins, R.N., 1987. Factors Influencing Stress Corrosion Crack Growth Kinetics. Corrosion 43, 130–139.

Provatas, N., Elder, K., 2011. Phase-Field Methods in Materials Science and Engineering. John Wiley & Sons.

Scully, J.C., 1980. The interaction of strain-rate and repassivation rate in stress corrosion crack propagation. Corrosion Science 20, 997–1016.